

Perfectly Matched Layers and Characteristic Boundaries in Lattice Boltzmann: Accuracy vs. Cost

Friedemann Klass *

University of Wuppertal, 42119 Wuppertal, Germany

Alessandro Gabbana †

*CCS-2 Computational Physics and Methods, Los Alamos National Laboratory, Los Alamos, 87545 New Mexico, USA
Center for Nonlinear Studies (CNLS), Los Alamos National Laboratory, Los Alamos, 87545 New Mexico, USA*

Andreas Bartel ‡

University of Wuppertal, 42119 Wuppertal, Germany

Artificial boundary conditions (BC) play a ubiquitous role in numerical simulations of transport phenomena in several diverse fields, such as fluid dynamics, electromagnetism, acoustics, geophysics and many more. They are essential for accurately capturing the behavior of physical systems whenever the simulation domain is truncated for computational efficiency purposes. Ideally, an artificial BC would allow relevant information to enter or leave the computational domain without introducing artifacts or unphysical effects. Boundary conditions designed to control spurious wave reflections are referred to as non-reflective boundary conditions (NRBC). Another approach is given by the perfectly matched layers (PML), in which the computational domain is extended with multiple dampening layers, where outgoing waves are absorbed exponentially in time.

In this work, we revise the definition of PML in the context of the lattice Boltzmann method. We evaluate and compare the impact of adopting different types of BC at the edge of the dampening zone, both in terms of accuracy and computational costs. We show that for sufficiently large buffer zones, PML allows stable and accurate simulations even when using a simple zero-th order extrapolation BC. Moreover, employing PML in combination with NRBC potentially offers significant gains in accuracy at a modest computational overhead, provided the parameters of the BC are properly tuned to match the properties of the underlying fluid flow.

*Ph.D. Candidate, University of Wuppertal, klass@math.uni-wuppertal.de

†Postdoctoral Researcher, Los Alamos National Laboratory, agabbana@lanl.gov

‡Lecturer, University of Wuppertal, bartel@math.uni-wuppertal.de

I. Introduction

The perfectly matched layer (PML) technique is an established tool to treat artificial boundaries that arise when truncating the physical domain of a given problem, allowing to limit the propagation of any unphysical activity in the bulk domain. Originally developed for the absorption of electromagnetic waves [1], the PML introduces a dampening zone beyond the artificial boundary in which a modified set of governing equations is solved. This modification ensures that i) outgoing waves decay exponentially and ii) the dampening zone is *perfectly* matched to the bulk in the sense that the interface between bulk and PML region will not cause reflections. A major advantage of the PML method is that it allows use of simple boundary conditions (BCs) beyond the dampening zone, as unphysical reflections arising at the boundary are absorbed by the dampening zone before they start interacting with the bulk. PMLs have been successfully applied to elastodynamics [2], the Schrödinger [3], Helmholtz [4], Euler [5–7] and Navier-Stokes [8–10] equations, as well as Boltzmann [11, 12] and lattice Boltzmann equations [13–15]. In addition to PML, other buffer-zone-like techniques have been developed for flow simulations, such as solution filtering in exit zones to reduce boundary reflections [16–18].

In the context of the lattice Boltzmann method (LBM) the definition of BC can represent a complex task, since they must be specified at the mesoscopic level, in terms of discrete particle distribution functions. Due to its simple implementation, PML is commonly employed in LBM simulations, in particular in the simulation of radiation [19] and acoustic phenomena [20, 21].

The LBM considered in this work is based on high order velocity stencils which support simulations of thermal compressible flow [22, 23]. These kind of lattices exhibit multiple layers of nodes, which further complicate the task of defining boundary conditions in terms of unknown values of (discrete) particle distribution functions. Under these settings, the conceptual advantage of the PML to enable use of simple BCs is even more appealing. Regardless of the order of the velocity stencils used, the dampening zone introduced in the method increases the computational cost, since the stream and collide paradigm of the LBM needs to be applied on an extended grid. This motivates the question whether the thickness of the dampening zone required to obtain a given level of accuracy can be minimized by employing non-reflecting BCs (NRBC) beyond the dampening zone. While the combination of PML and NRBC has been reported before [21], a thorough analysis investigating the trade-off between accuracy and computational costs is still missing. In this work we present an implementation of the PML combined with characteristic boundary conditions (CBC) [16] for the modelling of artificial boundaries. We compare this approach to the classical setup present in the literature [14], where the simple Zero Gradient (ZG) BC is used beyond the dampening zone. For both of these implementations, we evaluate the impact of the width of the dampening zone on both the obtained accuracy and the computational cost. We show that the combination of characteristic BCs with PML can provide significant gains in terms of accuracy, and at relatively modest computational overhead, provided that the parameters of both CBC and PML are carefully tuned. Moreover, when the accuracy provided by the ZG BC beyond the PML is sufficient, then the ZG BC offers simpler implementation and faster evaluation, even when using high-order multi-speed LBM models.

This work is structured as follows: Sec. II contains a brief description of the LBM. In Sec. III, we revisit in details the implementation of the PML, and its coupling with non-reflective BC. Subsequently, we present the BCs, which we combine with PML in order to enhance the boundary treatment in Sec. IV. Then, in Sec. V we discuss numerical results in which we evaluate the tread-off between accuracy and computational costs of different types of BC for a few standard numerical benchmarks. Finally, in Sec. VI we summarize our results and discuss possible future developments.

II. Lattice Boltzmann Method

The LBM [24, 25] is an established computational fluid dynamic solvers which, unlike traditional methods which explicitly discretize the Navier Stokes equations, makes use of a mesoscopic representation, solving a minimal version of the Boltzmann equation discretized on a Cartesian grid.

The description of the fluid fields is given in terms of a set of q discrete velocity distribution functions $f_i(\mathbf{x}, t) = f(\mathbf{x}, \mathbf{c}_i, t)$ (lattice populations hereafter), giving the probability of finding a particle with (discrete) velocity \mathbf{c}_i at the node of a Cartesian grid \mathbf{x} at time t .

The time evolution of the populations is governed by the discrete lattice Boltzmann-BGK equation

$$f_i(\mathbf{x} + \mathbf{c}_i \Delta t, t + \Delta t) = f_i(\mathbf{x}, t) + \Omega_i^{BGK} \quad i = 1, \dots, q, \quad (1)$$

where collisions are modeled using the single-relaxation time Bhatnagar-Gross-Krook (BGK) model [26]

$$\Omega_i^{BGK} = -\frac{1}{\tau} (f_i(\mathbf{x}, t) - f_i^{\text{eq}}(\mathbf{x}, t)),$$

where populations relax towards their local equilibrium state f_i^{eq} at rate τ .

The macroscopic hydrodynamic quantities are obtained from the velocity moments of the distribution. Working in rescaled units, where the Boltzmann constant k_b and the molecular mass m are set to unity, density ρ , velocity \mathbf{u} and internal energy density ρe are given as

$$\rho = \sum_{i=1}^q f_i, \quad \rho \mathbf{u} = \sum_{i=1}^q f_i \mathbf{c}_i, \quad d\rho e = \sum_{i=1}^q f_i |\mathbf{c}_i - \mathbf{u}|^2, \quad (2)$$

where d is the number of spatial dimensions. We consider here a mono-atomic gas and an ideal equation of state, thus the temperature T , internal energy e and hydrodynamic pressure P are put in relationship via [22]

$$e = \frac{d}{2} T, \quad P = \rho T c_s^2. \quad (3)$$

Using a multi-scale Chapman-Enskog expansion [27] it is possible to establish a link between the mesoscopic

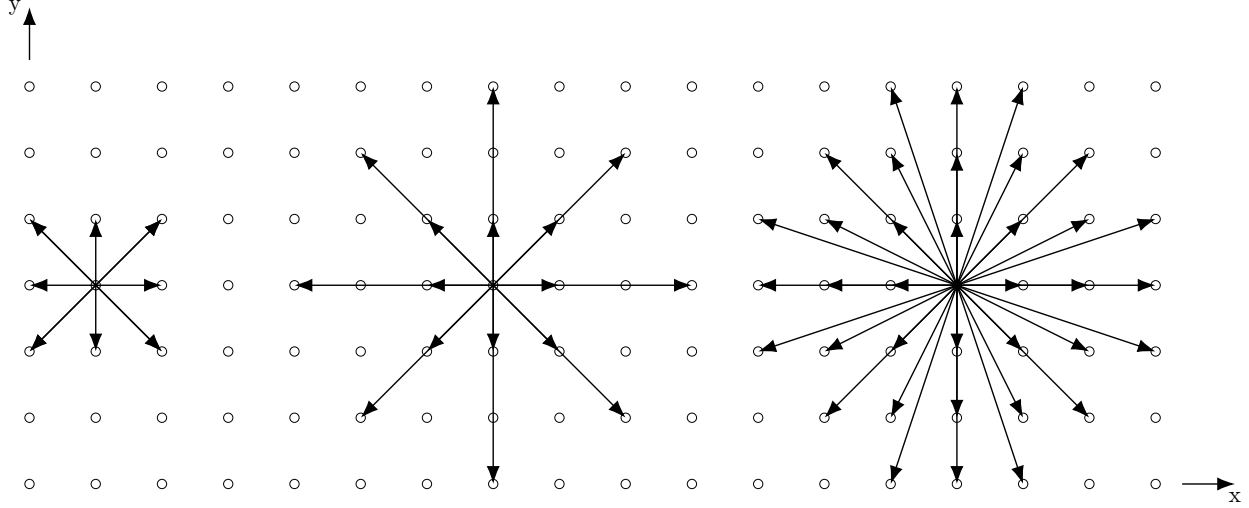


Fig. 1 Discrete velocities for the D2Q9 (left), D2Q17 (center) and D2Q37 (right) velocity stencils.

parameters and the kinematic viscosity ν

$$\nu = \left(\tau - \frac{1}{2} \right) c_s^2,$$

with c_s the lattice speed of sound.

Velocity stencils

To ensure that Eq. (2) holds, the discrete velocity stencil needs to be chosen according to the abscissa of a sufficiently high-order Gauss-Hermite quadrature [28] i.e., $\{(\omega_i, \mathbf{c}_i) : i = 1, \dots, q\}$, where ω_i are the quadrature weights. Different velocity stencils are commonly referred to using the $DdQq$ nomenclature, where d refers to the number of spatial dimensions and q to the number of discrete velocities.

In what follows we will restrict ourselves to the two-dimensional ($d = 2$) case, and consider the D2Q9, D2Q17 and D2Q37 stencils depicted in Fig. 1. While the commonly adopted D2Q9 model captures density and velocity, the underlying quadrature is not accurate enough to describe the temperature field [23, 29]. The D2Q17 velocity stencil can correctly recover the third order velocity moments of the particle distribution, however, it fails to capture the non-equilibrium component of the heat-flux [22], making it suitable only for simulations of mildly compressible flow. In contrast, the D2Q37 stencil enables simulations of fully compressible thermal flows. For the sake of computational efficiency, it is of interest to minimize the amount of discrete velocities. The velocity stencils here considered consist of the minimal amount of velocities required to form fifth-, seventh- and ninth-order quadrature rules, when additionally, non-negative weights and integer-valued velocities with a maximum displacement of $\mathcal{M} = 3$ are demanded [23].

An explicit expression for the equilibrium is obtained from an expansion in Hermite polynomials of the Maxwell-Boltzmann distribution [22]. Following the discussion in Ref. [23], we consider a second order expansion for the D2Q9

stencil,

$$f_i^{\text{eq},2}(\rho, \mathbf{u}, T) = \omega_i \rho \left(1 + \mathbf{u} \cdot \mathbf{c}_i + \frac{1}{2c_s^2} [(\mathbf{u} \cdot \mathbf{c}_i)^2 - u^2 + (T-1)(c_i^2 - 2)] \right), \quad (4)$$

a third order expansion for the D2Q17 stencil,

$$f_i^{\text{eq},3}(\rho, \mathbf{u}, T) = f_i^{\text{eq},2}(\rho, \mathbf{u}, T) + \omega_i \rho \frac{\mathbf{u} \cdot \mathbf{c}_i}{6c_s^4} \left((\mathbf{u} \cdot \mathbf{c}_i)^2 - 3u^2 + 3(T-1)(c_i^2 - 4) \right), \quad (5)$$

and a fourth order expansion for the D2Q37 stencil

$$f_i^{\text{eq},4}(\rho, \mathbf{u}, T) = f_i^{\text{eq},3}(\rho, \mathbf{u}, T) + \omega_i \rho \frac{1}{24c_s^6} \left((\mathbf{u} \cdot \mathbf{c}_i)^4 - 6(\mathbf{u} \cdot \mathbf{c}_i)^2 u^2 + 3u^4 + 6(T-1)((\mathbf{u} \cdot \mathbf{c}_i)^2 (c_i^2 - 4) + |\mathbf{u}|^2 (4 - c_i^2)) + 3(T-1)^2 (c_i^4 - 8c_i^2 + 8) \right), \quad (6)$$

respectively, where $u^2 = \mathbf{u} \cdot \mathbf{u}$, $c_i^2 = \mathbf{c}_i \cdot \mathbf{c}_i$ and the speed of sound c_s is a lattice specific constant.

We conclude this section by outlining the algorithm for solving Eq. 1. First, the the discrete distribution f_i are initialized, for example according to the equilibria (Eq. (4)-(6)) evaluated at desired macroscopic fields. Each time step consists of 1) evaluation of the collision operator (right hand side of Eq. 1) and 2) streaming step in which populations are moved to neighboring nodes according to the directions defined by the velocity stencil. Unless working on a fully periodic domain, the streaming step will leave post-streaming populations at boundary nodes unspecified, thus requiring employing suitable BC for defining missing populations before updating the macroscopic values by means of Eq. (2) and proceeding to the next iteration.

III. Perfectly Matched Layers

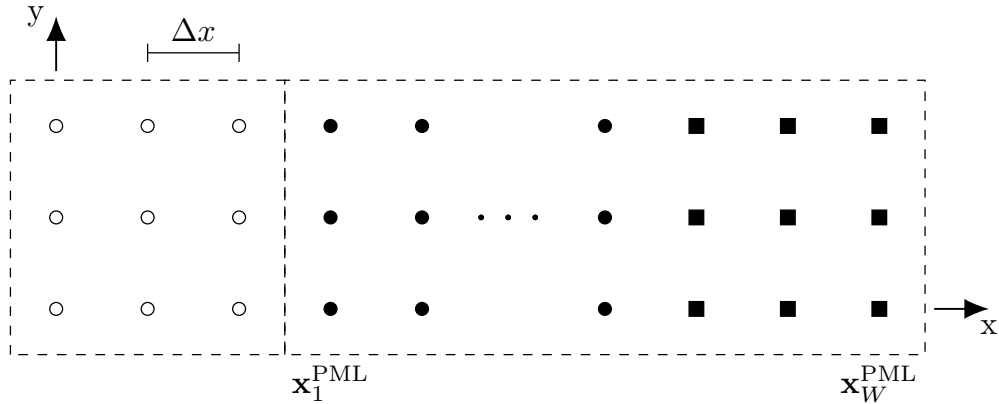


Fig. 2 Sketch of PML geometry for a right-hand side boundary on an equidistant grid.

In this section we summarize the derivation of PML for LBM, following the approach originally presented in

Ref. [14]. The general idea of PML consists in extending the computational domain introducing a dampening layer where governing equations are modified such that reflection waves are damped out and (ideally) no reflections arise at the interface. In Fig. 2 we sketch the PML geometry for a right-hand side boundary. In the figure, the bulk region (hollow nodes) is padded with W layers (filled nodes), where a modified governing equation is solved. The flow in the absorbing zone is dampened towards a mean equilibrium state, in turn enabling use of standard boundary conditions at the edge of the computational domain (square nodes).

For the implementation of this concept at the in the mesoscale LBM framework, the starting point is the splitting of the particle distribution f_i as the sum of an equilibrium term f_i^{eq} and a non-equilibrium component f_i^{neq}

$$f_i = f_i^{\text{eq}} + f_i^{\text{neq}} = \bar{f}_i^{\text{eq}} + \hat{f}_i^{\text{eq}} + f_i^{\text{neq}}, \quad (7)$$

where f_i^{eq} is further decomposed into a (global) mean equilibrium component \bar{f}_i^{eq} and a deviation from the mean equilibrium \hat{f}_i^{eq} . The PML approach aims at suppressing the fluctuations contained in \hat{f}_i^{eq} . That is, the flow is driven towards a prescribed mean equilibrium state \bar{f}_i^{eq} in the dampening region, absorbing reflections occurring at boundary nodes.

Starting from the discrete velocity Boltzmann-BGK equation in two spatial dimensions

$$\frac{\partial f_i}{\partial t} + c_{i,x} \frac{\partial f_i}{\partial x} + c_{i,y} \frac{\partial f_i}{\partial y} = \Omega_i^{\text{BGK}}, \quad (8)$$

we introduce non-negative dampening coefficients [2, 7], σ_x and σ_y respectively along the x and y component, which in combination with Eq. 7 allow to cast the LHS of Eq. 8 as

$$\frac{\partial \hat{f}_i^{\text{eq}}}{\partial t} + c_{i,x} \frac{\partial \hat{f}_i^{\text{eq}}}{\partial x} + c_{i,y} \frac{\partial \hat{f}_i^{\text{eq}}}{\partial y} = - \underbrace{\left[\sigma_y c_{i,x} \frac{\partial Q_i}{\partial x} + \sigma_x c_{i,y} \frac{\partial Q_i}{\partial y} + (\sigma_x + \sigma_y) \hat{f}_i^{\text{eq}} + \sigma_x \sigma_y Q_i \right]}_{:= \Omega_i^{\text{PML}}}, \quad (9)$$

with Q_i defined as

$$\frac{\partial Q_i}{\partial t} = \hat{f}_i^{\text{eq}}. \quad (10)$$

It follows that due to the decomposition in Eq. 7 the PML can be expressed as a modification of the collision term:

$$\frac{\partial f_i}{\partial t} + c_{i,x} \frac{\partial f_i}{\partial x} + c_{i,y} \frac{\partial f_i}{\partial y} = \Omega_i^{\text{BGK}} + \Omega_i^{\text{PML}}. \quad (11)$$

Hereafter we assume $\sigma_x = \sigma_y = \sigma$. This choice, which allows to simplify Ω_i^{PML} down to

$$\Omega_i^{\text{PML}} = -\sigma \left(\mathbf{c}_i \cdot \nabla Q_i + 2\hat{f}_i^{\text{eq}} + \sigma Q_i \right), \quad (12)$$

proves to be beneficial in terms of numerical stability [14]. The absorption coefficient σ controls the strength of the dampening effect of the PML. We remark that σ is not necessarily a constant but may vary spatially and in time. In this work, we restrict our analysis to one specific case, and follow the common practice [11] of ramping up the absorption coefficient σ quadratically with respect to the distance from the interface. Formally, the dampening strength in the i -th level of nodes in the PML (cf. Fig. 2) is given by

$$\sigma(\mathbf{x}_i^{\text{PML}}) = \sigma_{\max} \left(\frac{i}{W} \right)^2, \quad i = 1, 2, \dots, W, \quad (13)$$

where W is the depth of the PML. Therefore, in our analysis W and σ_{\max} will be the free parameters of the PML, which can be tuned for optimized accuracy and stability [30].

After discretization of space and time, the implementation of the PML for LBM is as follows. In the bulk, the usual lattice Boltzmann-BGK equation Eq. (1) is evolved. In the dampening zone, the collision operator is modified by adding Eq. (12), thus the governing equation reads as

$$f_i(\mathbf{x} + \mathbf{c}_i \Delta t, t + \Delta t) = f_i(\mathbf{x}, t) + \Omega_i^{\text{BGK}}(\mathbf{x}, t) + \Omega_i^{\text{PML}}(\mathbf{x}, t). \quad (14)$$

We use the trapezoidal rule to evaluate the quantity Q_i in Eq. (10)

$$Q_{i,t+\Delta t} = \frac{1}{2} \left(\hat{f}_{i,\Delta t}^{\text{eq}} + f_{i,t+\Delta t}^{\text{eq}} - \tilde{f}_{i,t+\Delta t}^{\text{eq}} \right),$$

while its spatial gradients are evaluated using second order finite differences, specifically we use one-sided differences at the outermost layer of nodes $\mathbf{x}_W^{\text{PML}}$

$$\frac{\partial Q_i(\mathbf{x}_{b,M})}{\partial \alpha} \approx \frac{1}{2} (3Q_i(\mathbf{x}) - 4Q_i(\mathbf{x} - \Delta x \mathbf{e}_\alpha) + Q_i(\mathbf{x} - 2\Delta x \mathbf{e}_\alpha)). \quad (15)$$

while central finite differences are used for all other cases

$$\frac{\partial Q_i(\mathbf{x}_{b,j})}{\partial \alpha} \approx \frac{1}{2} (Q_i(\mathbf{x} + \Delta x \mathbf{e}_\alpha) - Q_i(\mathbf{x} - \Delta x \mathbf{e}_\alpha)), \quad (16)$$

where α is the spatial index and \mathbf{e}_α the outward facing normal vector corresponding to the boundary.

We stress once again that the action of the PML in LBM is entirely contained in the modified collision operator

appearing in Eq. (12), thus preserving the the stream and collide paradigm of the numerical method.

IV. Boundary Conditions

The implementation of the PML described in the previous section still requires that a boundary condition is specified at the outer-most layer of the absorbing zone. Since the PML absorbs reflections occurring at the boundaries, in principle even very crude and simple BCs can be employed in combination with PML. However, the grid extension introduced by the dampening zone leads to increase in computational costs, and we are here interested in investigating whether the choice of the BC applied at the edge of the dampening zone can be used to minimize the PML width W , still yielding a desired level of accuracy. In our analysis we will consider two types of BC, respectively a simple zero-gradient BC and a non-reflective BC, which are below detailed.

Zero Gradient

The zero-gradient BC (ZG) represents arguably the simplest possible choice for an outflow BC. Here populations at the boundary nodes $\mathbf{x}_{b,j}$, $j = 1, 2, \dots, \mathcal{M}$ are obtained with a zero-th order extrapolation from the adjacent fluid node \mathbf{x}_f :

$$f_i(\mathbf{x}_{b,j}, t + \Delta t) = f_i(\mathbf{x}_f, t + \Delta t) \quad i = 1, 2, \dots, q. \quad (17)$$

Characteristic BC

We consider recently developed characteristic BC [31, 32] (CBC) for LBM, which allows to modulate incoming wave amplitudes by considering an hyperbolic approximation of the target governing macroscopic equations. We summarize below the two main ingredients in the derivation of CBC.

Characteristic Analysis

Starting from a macroscopic transport equation (Navier-Stokes-Fourier in our case, providing the time evolution of the macroscopic fields $\mathbb{U} := (\rho, u_x, u_y, T)^\top$), one aims at casting the equation in the following form

$$\frac{\partial \mathbb{U}}{\partial t} = -A \frac{\partial \mathbb{U}}{\partial x} + \mathbb{T} + \mathbb{V}. \quad (18)$$

In the above, \mathbb{T} and \mathbb{V} represent transversal and viscous contributions. Upon discarding these contributions, Eq.18 simplifies down to the so-called locally one dimensional inviscid (LODI) approximation, which allows for analyzing the amplitude variations of waves crossing the boundary. This analysis can be performed by first diagonalizing $A = S^{-1}\Lambda S$, and next by identifying the amplitude variations of waves crossing the boundary via

$$\mathcal{L}_x = \left(\mathcal{L}_{x,1}, \mathcal{L}_{x,2}, \mathcal{L}_{x,3}, \mathcal{L}_{x,4} \right)^\top = \Lambda S \frac{\partial \mathbb{U}}{\partial x}, \quad (19)$$

where the sign of Λ_{ii} determines the propagation direction the i -th wave. Thus, it is possible to distinguish between waves entering and leaving the computational domain. This makes it possible to replace the vector \mathcal{L}_x with a modified vector $\bar{\mathcal{L}}_x$, where amplitudes of outgoing waves are retained and incoming wave amplitudes are manipulated.

Variations of characteristic BCs

Several variations of characteristic BCs can be identified depending on how incoming wave amplitudes $\bar{\mathcal{L}}_{x,\text{inc}}$ are treated. In a perfectly non-reflecting boundary condition, they are simply set to zero [33],

$$\bar{\mathcal{L}}_{x,\text{inc}} = 0. \quad (20)$$

However, this in practice often leads to a drift in the macroscopic target quantities in the long term. Imposing a relaxation of target macroscopic quantities towards a reference state [34] offers a (partial) remedy to the problem.

Once $\bar{\mathcal{L}}_x$ is specified, the hyperbolic approximation to Eq. (18) reads [35]

$$\frac{\partial \mathbb{U}}{\partial t} = -S^{-1} \bar{\mathcal{L}}_x + \mathbb{T} + \mathbb{V} = -S^{-1} (\bar{\mathcal{L}}_x + \mathcal{T} + \mathcal{V}), \quad (21)$$

In the spirit of the LODI approximation used to compute $\bar{\mathcal{L}}$, the so-called LODI BC is obtained by dropping transversal and viscous contributions [36], where the macroscopic system reads

$$\frac{\partial \mathbb{U}}{\partial t} = -S^{-1} \bar{\mathcal{L}}_x. \quad (22)$$

Numerically solving either Eq. (21) or (22) yields macroscopic target values \mathbb{U}_{tgt} (see Ref. [32] for details).

Finally, it is possible to use \mathbb{U}_{tgt} to implement a mesoscopic Dirichlet BC. We consider here the non-equilibrium extrapolation method

$$f_i(\mathbf{x}_{b,j}, t + \Delta t) = f_i^{\text{eq}}(\rho_{\text{tgt}}, \mathbf{u}_{\text{tgt}}, T_{\text{tgt}}) + f_i^{\text{neq}}(\mathbf{x}_f, t + \Delta t)$$

where the non-equilibrium part of populations at the boundary nodes $\mathbf{x}_{b,j}$, $j = 1, 2, \dots, \mathcal{M}$ is copied from the nearest fluid node \mathbf{x}_f (see e.g. Ref. [37] for a discussion on other possible choices for multi-speed LBM).

Finally, we remark that it is in principle possible to include the extra terms introduced by the PML in the characteristic analysis (see Appendix VI.A for details).

V. Numerical Results

In this section we report our numerical results, evaluating accuracy and computational costs of employing PML in combination with different underlying BC, also varying the free parameters offered by the PML/BC. We consider

two standard numerical benchmarks often employed in the evaluation of artificial boundaries [21, 32, 35], namely a mono-dimensional type of flow triggered by an initial density step, in Sec. V.A, and the propagation of a vortex out of the computational domain in Sec. V.B. We start by detailing the performance metrics and how we established reference data.

Reference Simulation

The accuracy of the BCs is quantified by computing errors with respect to reference fields. Such reference fields Z^{ref} are obtained from a fully periodic LBM simulation on an extended grid for the quantities $Z \in \{\rho, u_x, u_y, T\}$. The reference simulation is conducted on a grid sufficiently large such that no interaction takes place between the boundaries and the bulk dynamics in the region of interest, ensuring that the only possible source of error lies in the boundary treatment.

In what follows we will report global relative L^2 -errors e_Z and pointwise relative L^2 -errors \tilde{e}_Z with respect to the reference fields, which we compute as

$$e_Z = \left(\sum_{(x,y) \in L_x \times L_y} \left(\frac{|Z(x,y) - Z^{\text{ref}}(x,y)|}{|Z^{\text{ref}}(x,y)|} \right)^2 \right)^{\frac{1}{2}}, \quad \tilde{e}_Z(x,y) = \frac{|Z(x,y) - Z^{\text{ref}}(x,y)|}{|Z^{\text{ref}}(x,y)|}.$$

Moreover, we also define an average global error \bar{e}_Z , computed by averaging e_Z over all the iterations sampled. Finally, we also introduce the quantity C_Z to compare the average error of a specific implementation against the one obtained employing the ZG BC:

$$C_Z = \frac{\bar{e}_Z}{\bar{e}_Z^{\text{ZG}}}, \quad Z \in \{\rho, u_x, u_y, T\}. \quad (23)$$

Computational Cost

In a typical LBM simulation, the cost of evaluation the BC at the edges of the computational domains is typically negligible with respect to the total execution time, specially for large grid sizes. In order to establish a fair comparison between the different BC schemes, in our analysis we measure the (wall clock) time t^{BC} spent in computing kernels devoted to the processing of boundary conditions. If the PML is used, this will also includes the time required for the additional stream collide operations in the dampening zone. In what follows we will indicate with C_t the relative increase in the cost of processing boundary nodes with respect to execution time required for evaluating the ZG BC, i.e.

$$C_t = \frac{t^{\text{BC}}}{t^{\text{ZG}}}. \quad (24)$$

A. One-dimensional density step test case

We consider a flow with a one-dimensional dynamic, with initial conditions given by a homogeneous background velocity $\mathbf{u}_0 = (u_x, 0)$ (parallel to the x -axis) and a smooth density step given by

$$\rho(x, y) = \begin{cases} \rho_1 + \frac{\rho_1 - \rho_0}{2} \left(\tanh \left(s \left(x - \frac{1}{4} L_x \right) - 1 \right) \right), & \text{if } x \leq \frac{L_x}{2}, \\ \rho_1 - \frac{\rho_1 - \rho_0}{2} \left(\tanh \left(s \left(x - \frac{3}{4} L_x \right) - 1 \right) \right), & \text{else,} \end{cases} \quad (25)$$

where the parameter s controls the steepness of the initial step. We perform simulations on a grid of size $L_x \times L_y = 200 \times 20$. Numerical values for the parameters are $\rho_0 = 1$, $\rho_1 = 1.05$, $s = 0.5$ and the background velocity is determined from the Mach number, which is here set to $\text{Ma} = 0.05$.

The left- and right-hand side boundaries of the rectangular domain are equipped with artificial BC, while upper and lower boundaries are periodic. In this benchmark, the mean equilibrium \bar{f}^{eq} used in the PML domain is computed with respect to the quantities ρ_0 , \mathbf{u}_0 . The perfectly non-reflecting LODI BC based on Eqs. (20) and (22) is used as a characteristic BC.

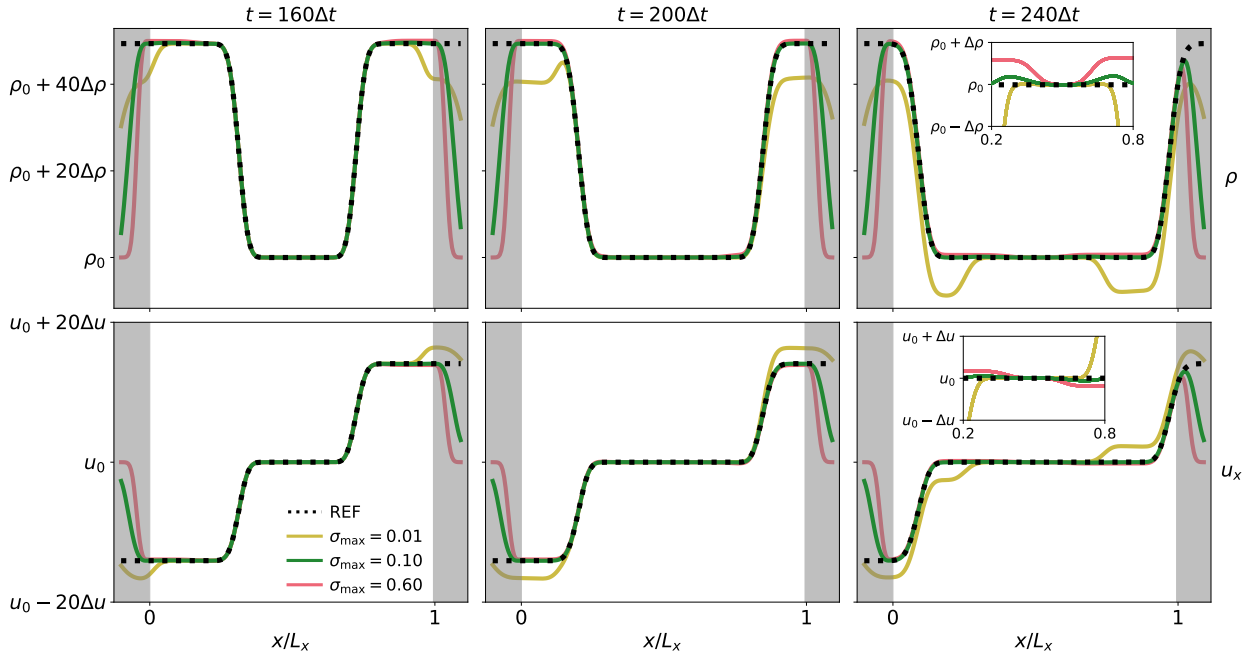


Fig. 3 Time evolution of the density ρ and x -component of the velocity field u_x for the “density step” test case. Numerical values for the axis extent are $\Delta\rho = 0.0005$, $\Delta u = 0.001$.

The effect of the dampening zone on the flow fields can be observed from Fig. 3, where profiles of the density and stream-wise velocity are shown for selected time steps along the horizontal midplane $y = L_y/2$, and the ZG BC is used beyond the PML. In the figure, the gray-colored areas at the left and right hand of the domain represent $W = 20$ additional layers of nodes used by the PML. We compare the reference solution (dotted lines), obtained on an extended

grid, with simulations on the reduced domain using different values of $\sigma_{\max} = \{0.01, 0.10, 0.60\}$ to highlight the importance of carefully selecting the value of the dampening rate. When σ_{\max} is too small ($\sigma_{\max} = 0.01$ in our example), the dampening effect is not sufficiently strong to absorb the reflections originating from the ZG BC, which are seen polluting the bulk domain. On the other hand, taking a larger value $\sigma_{\max} = 0.60$ leads to a more rapid decay towards the macroscopic values imposed by \bar{f}^{eq} in the dampening zone. However, this creates a mismatch at the interface with an overshooting of the macroscopic fields in the bulk of the domain (cf. inset in Fig 3). Finally, we show that it is possible to find an optimal value, $\sigma_{\max} = 0.10$, which allows to minimize the impact of the reflection waves of the bulk dynamic.

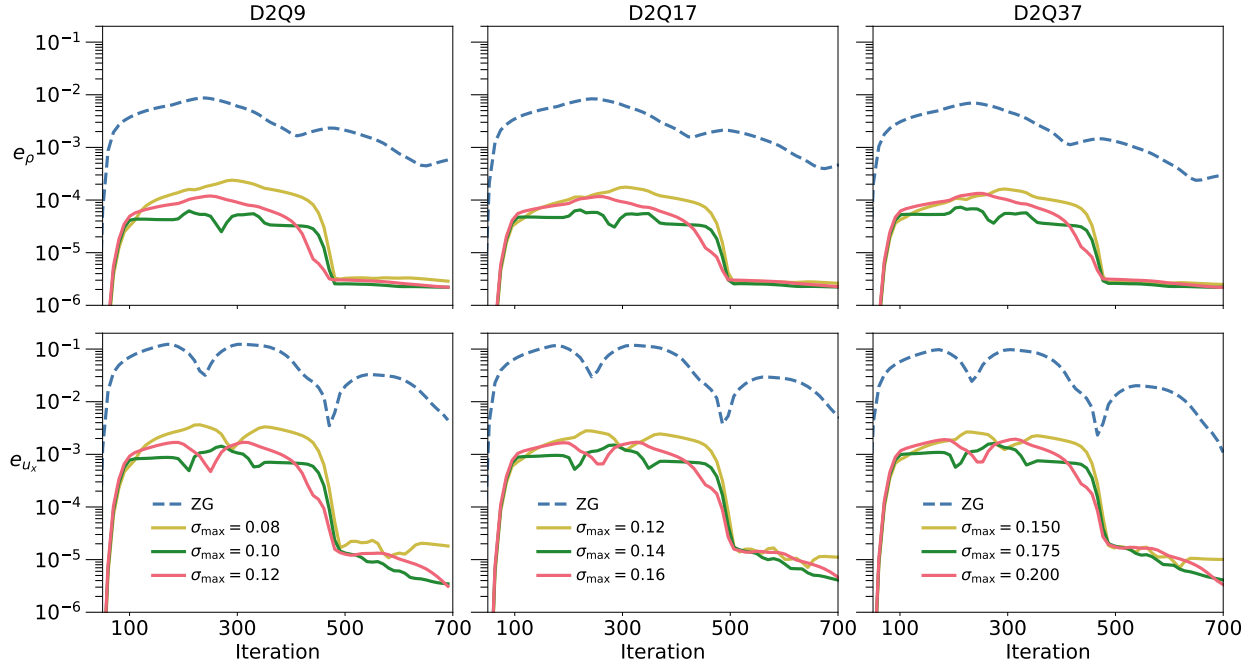


Fig. 4 Time evolution of global errors for density (top row) and velocity (bottom row) for the “density step” benchmark, using ZG BC.

On a more quantitative ground, in Fig. 4 we report the time evolution of global relative L^2 -errors e_Z , for the three different stencils employed in this work, and for different values of σ_{\max} . We show that combining ZG with PML reduces the global errors e_Z by about two orders of magnitude over the pure ZG BC without any dampening layers (dashed line in the figure). The level of accuracy is comparable for both the single speed D2Q9 model, and the multi-speed D2Q17 and D2Q37. The optimal value of σ_{\max} , which is critical for overall accuracy, was determined by a parameter scan, and it is found to depend on the value W , the velocity stencil, and on the BC used at the outer-most layer of the PML. In Fig. 5 we report a similar analysis, this time comparing ZG and LODI BC, with (solid lines) and without (dashed lines) PML, for the D2Q17 velocity stencil. The dampening coefficients used for the data reported in the figure are respectively $\sigma_{\max} = 0.08$ for LODI and $\sigma_{\max} = 0.14$ for ZG.

We observe that for a fixed value of $W = 20$, the accuracy obtained using the LODI BC beyond the PML is

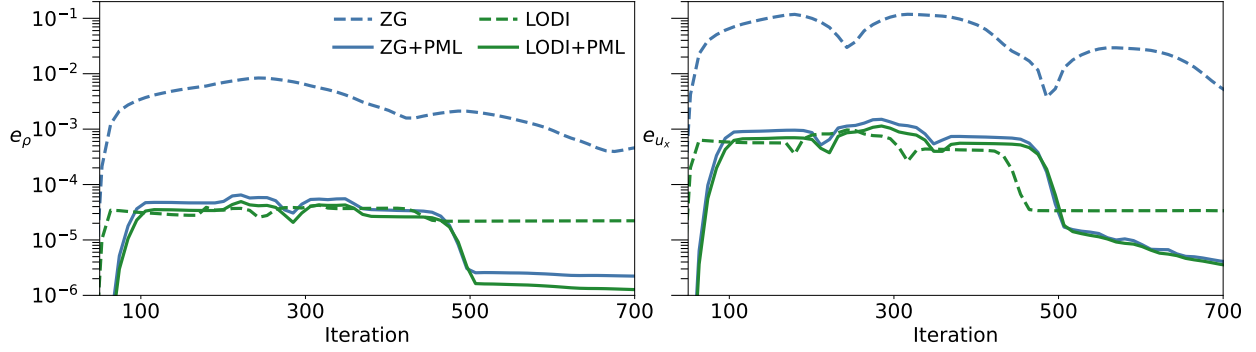


Fig. 5 Time evolution of the global errors for density (left) and velocity (right) fields for the “density step” benchmark, comparing ZG and LODI for the D2Q17 model.

approximately the same as for the ZG BC case. Moreover, the LODI BC without PML is able to match the accuracy of PML (and even minimize the maximum error) up until the end of the interaction of the density step with the boundary. Afterwards, the PML drives the flow to the correct steady state defined by $\bar{f}^{\text{eq}}(\rho_0, \mathbf{u}_0)$, yielding improved accuracy over non-PML BCs in the later stages of the numerical simulation.

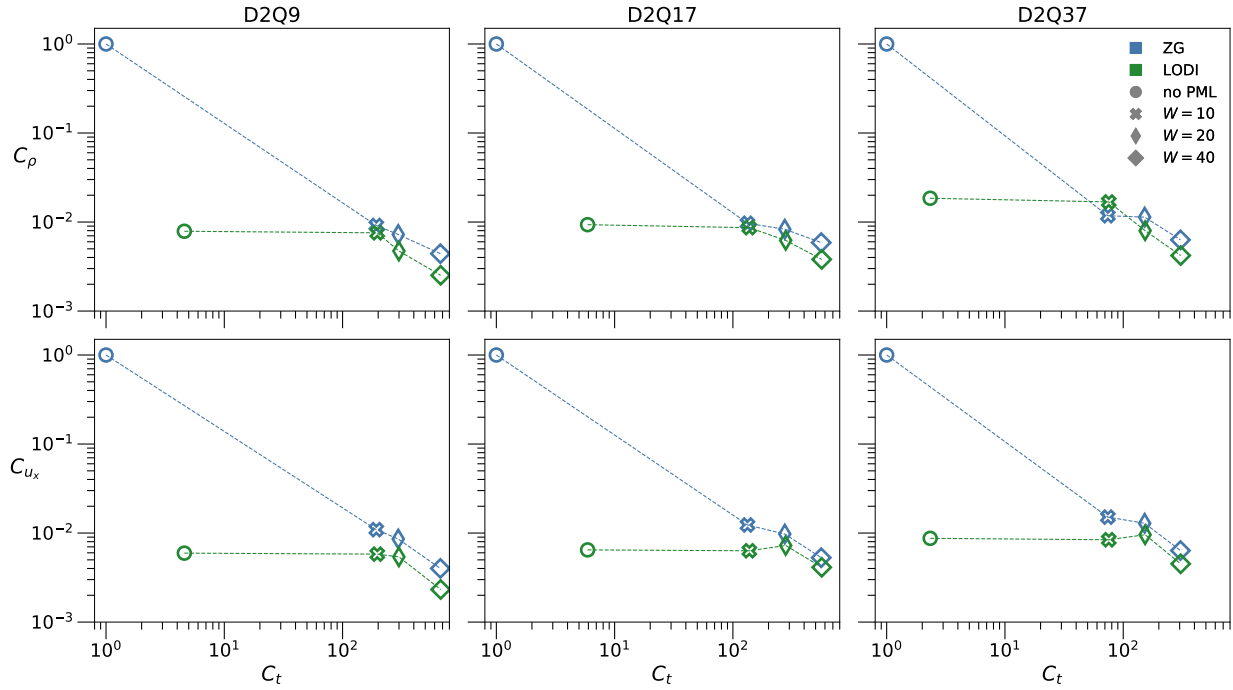


Fig. 6 Computational cost vs accuracy for the “density step” test case. See text for definition of the error metric C_Z and scaled computational cost C_t .

We conclude the analysis for this first benchmark considering the trade-off between computational cost and accuracy of the boundary treatment. In Fig. 6 we report the quantity C_t (cf. Eq (23)) vs C_Z (cf. Eq. (24)), i.e. the relative global error and relative computational cost of the BC computing kernels scaled with respect to data for the ZG BC without

PML. The values of dampening coefficient σ_{\max} used in the different cases are tabulated in Table 1.

Table 1 Values of σ_{\max} used for the “density step” test case. We report PML-BC combinations with varying PML thickness W in dependence of the underlying discrete velocity stencil.

BC	D2Q9			D2Q17			D2Q37		
	W=10	W=20	W=40	W=10	W=20	W=40	W=10	W=20	W=40
ZG	0.17	0.10	0.07	0.33	0.14	0.09	0.35	0.175	0.10
LODI	0.001	0.04	0.04	0.001	0.08	0.04	0.001	0.10	0.06

Since the flow in this benchmark presents a strictly one-dimensional dynamic, the assumptions made in the definition of the LODI BC are satisfied and allow to deliver a good level of accuracy even without PML (two orders of magnitude over the ZG BC regardless of the chosen velocity stencil), at a modest computational overhead. The introduction of a dampening zone of $W = 10$ nodes beyond each horizontal boundary in the PML approach increases the computational cost of evaluating the boundary nodes by about two order of magnitude, independently of the underlying velocity stencil. The overhead comes from the need of applying the stream and collide paradigm to the PML nodes. Evolving the fluid in the dampening zone becomes the dominant cost factor of the boundary treatment even at moderate thickness values W , as for a given value of W , the runtime of all PML/BC combinations is comparable.

Employing a thin PML consisting of $W = 10$ nodes on each lateral boundary, the ZG BC gives very similar accuracy to the LODI scheme. Using the LODI scheme in conjunction with PML or a wider PML zone with the ZG BC gives only small improvements in accuracy while increasing the simulation time. Thus, for such a simple flow configuration, the usage of characteristic BCs without PML appears to be the most efficient choice.

The values of σ_{\max} used in the simulations performed to carried the analysis are reported in Tab. 1, and they show that since the LODI scheme is capable of significantly damping reflection waves it requires smaller values of σ_{\max} than the ZG BC.

B. Propagating vortex test case

We consider a second benchmark, this time with a fully two-dimensional dynamic, to further put under stress the CBC scheme. We consider the propagation of a thermal vortex in a rectangular computational domain of size $L_x \times L_y$. The initialization of the problem is given in terms of normalized spatial coordinates $(x^*, y^*) \in [-1, 1]^2$:

$$x^* = \frac{2(x-1)}{L_x-1} - 1, \quad y^* = \frac{2(y-1)}{L_y-1} - 1.$$

The homogeneous background flow fields are given as

$$\rho(x, y) = \rho_0, \quad \mathbf{u}(x, y) = \mathbf{u}_0 = \begin{pmatrix} u_{0,x} \\ 0 \end{pmatrix}, \quad T(x, y) = T_0$$

and $u_{0,x}$ is determined from the Mach number which is set to $\text{Ma} = 0.1$.

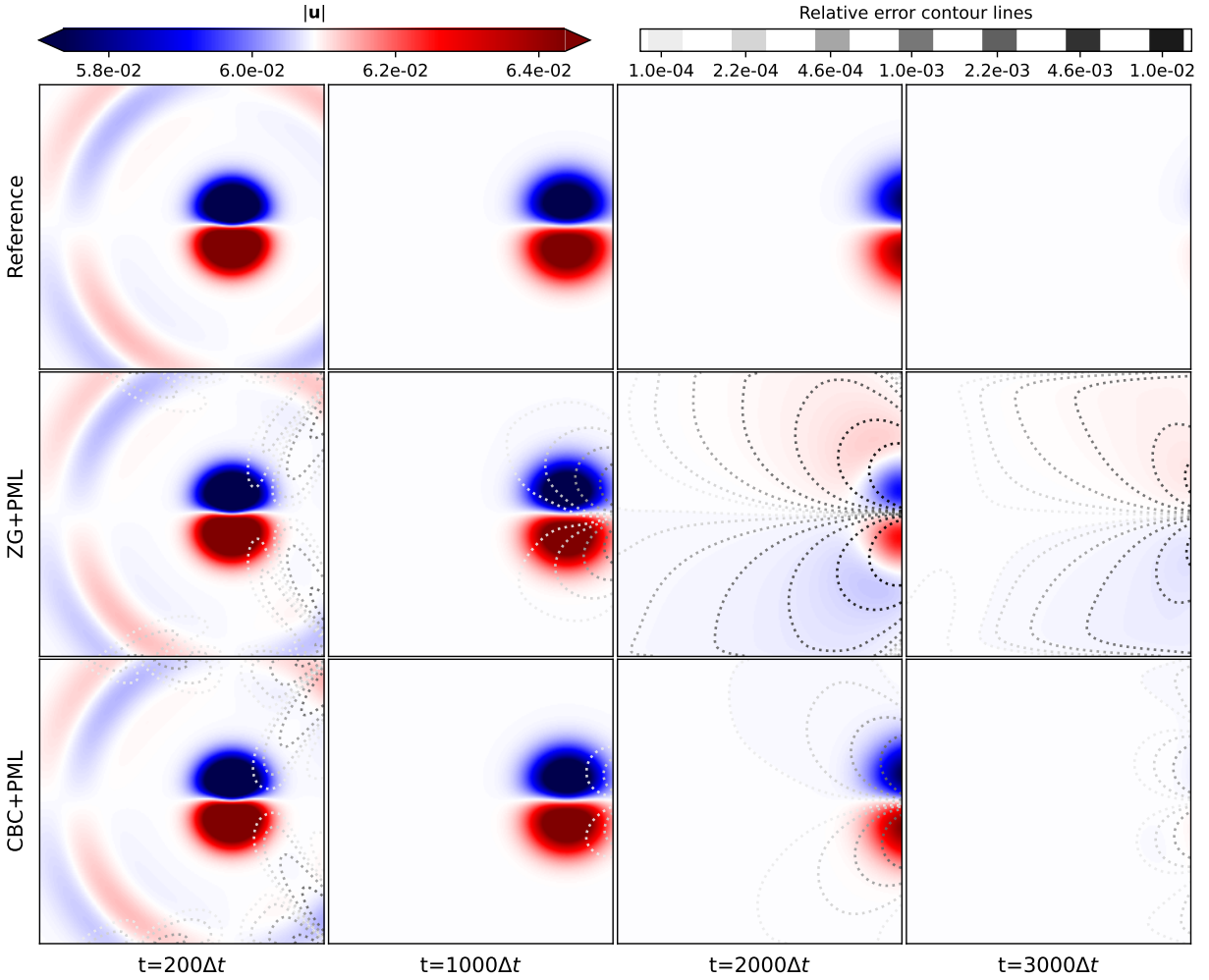


Fig. 7 Time evolution of the magnitude of the velocity field for the thermal vortex benchmark.

The thermal vortex is formed by a perturbation of both temperature and velocity within a circle centered at $(x_0^*, 0)$ and with radius r^* . The center of the vortex $x_0^* = \frac{K}{L_x - 1}$ is given in terms of a parameter K , that defines the displacement

along the horizontal midplane. More precisely, the initial velocity and temperature fields read

$$\mathbf{u}(x, y) = \mathbf{u}_0 + \begin{cases} 0, & \text{if } (x^* - x_0^*)^2 + y^{*2} \geq r^{*2} \\ \mathbf{v}(x^* - x_0^*, y^*) & \text{otherwise,} \end{cases} \quad T(x, y) = T_0 + \begin{cases} 0 & \text{if } (x^* - x_0^*)^2 + y^{*2} \geq r^{*2}, \\ \theta(x^* - x_0^*, y^*) & \text{otherwise,} \end{cases}$$

In the above, the vortex strength in terms of the initial perturbations is given in terms of a shape parameter b as

$$\mathbf{v}(x, y) = \frac{5}{2}u_{0,x}2^{-\frac{x^2+y^2}{b^2}} \begin{pmatrix} y \\ -x \end{pmatrix}, \quad \theta(x, y) = y \frac{5}{2}u_{0,x}2^{-\frac{x^2+y^2}{b^2}}. \quad (26)$$

The Eckert number corresponding to the simulation parameters is $Ec \approx 0.02$.

This benchmark is more challenging with respect to the BC, as a flow with fully two-dimensional dynamics is simulated. Thus, reflections may occur at an arbitrary angle. Here, all the boundaries are considered as open boundaries and thus, the entire computational domain is padded with an absorbing zone of width W , giving an effective grid size of $(L_x + 2W) \times (L_y + 2W)$. In what follows we use $L_x = L_y = 300$ and the D2Q17 stencil.

In order to employ characteristic BCs, incoming wave amplitude variations need to be posed at the boundaries. Following [38], the outlet is treated using the CBC given by Eq. (21), where the incoming wave amplitude at the velocity outlet at the right-hand side boundary is posed as

$$\bar{\mathcal{L}}_{x,i} = (1 - Ma)\bar{\mathcal{T}}_{x,i} + \mathcal{V}_{x,i}. \quad (27)$$

Other straight edge boundary are treated using the perfectly non-reflecting LODI BC given by Eqs. (20) and (22). Figure 7 provides snapshots at different time steps of the magnitude of the velocity field, comparing the dynamic obtained on a reference grid with that provided by PML with $W = 10$ nodes in combination with ZG BC (middle row), and with the CBC (bottom row). The maximum dampening strength was set to $\sigma_{\max} = 0.02$ for the ZG BC and $\sigma_{\max} = 0.007$ for the CBC.

We observe that right after initialization, a spherical pressure pulse starts traveling through the bulk domain, causing interactions with the open boundaries, which are visible already at $t = 200\Delta t$ (in particular in proximity of corner nodes). After $1000\Delta t$ iterations, the core of the vortex begins interacting with the boundary. From here on, the ZG BC introduces significant reflection waves which pollute the results in the bulk domain. On the other hand, the entire vortex-boundary interaction is more accurately captured if the CBC is used over the ZG BC at the outlet.

In Fig. 8, the errors caused by the boundary treatment are quantified over the course of the simulation by tracking the time evolution of e_Z for different macroscopic fields. Once again, in the figure we use dashed lines to denote the ZG BC

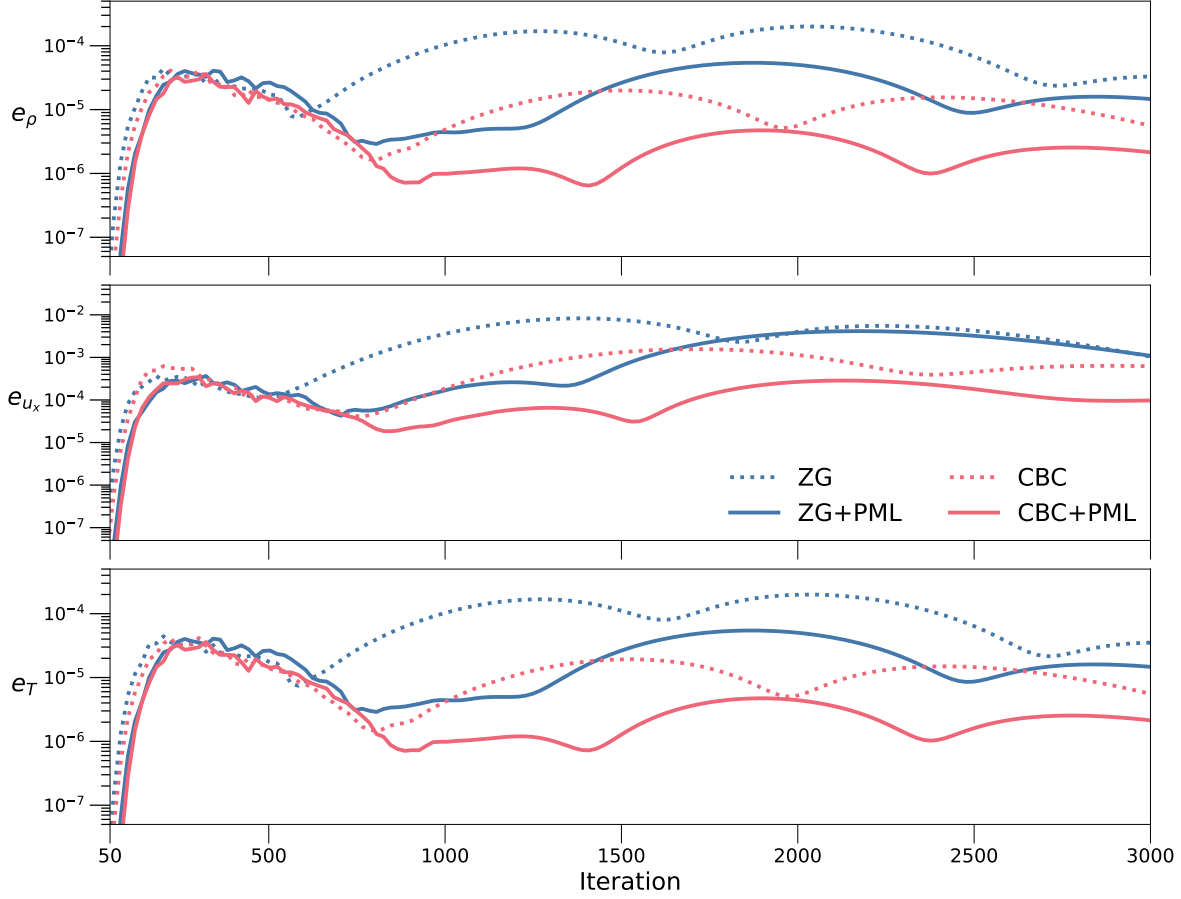


Fig. 8 Time evolution of the global errors for density (top row) x -component of the velocity (middle row) and temperature field (bottom row) for the “thermal vortex” benchmark.

(blue) and the CBC BC (red) without PML, while continuous lines show results for ZG and CBC combined with PML.

As expected, the large errors are observed when using the plain ZG BC without PML. Combining the ZG BC with a PML of width $W = 10$ leads to a level of accuracy comparable to that of the characteristic BC without PML. The accuracy can be further improved by combining CBC with PML.

The computational cost for this gain in accuracy is inspected in Fig. 9, where we present the relative increase in runtime vs the obtained accuracy for the PML used at several values of W in conjunction with the various BCs. Likewise for the previous benchmark, the optimal value for σ_{\max} was obtained by performing a parameter scan (and the cost of this scan is not taken into account in the analysis). They are given by, respectively for the ZG (CBC) BC 0.02(0.007) for $W = 10$, 0.01(0.002) for $W = 20$, and 0.003(0.001) for $W = 40$.

In order to evaluate the impact of the choice of how the incoming wave amplitudes are modulated, we compare two different CBC schemes. The first one, which has been used so far, and which we here label CBC (A), employs the relaxation scheme described by Eq. 27. The second, CBC (B) uses instead the perfectly non-reflecting version given by Eq. 20.

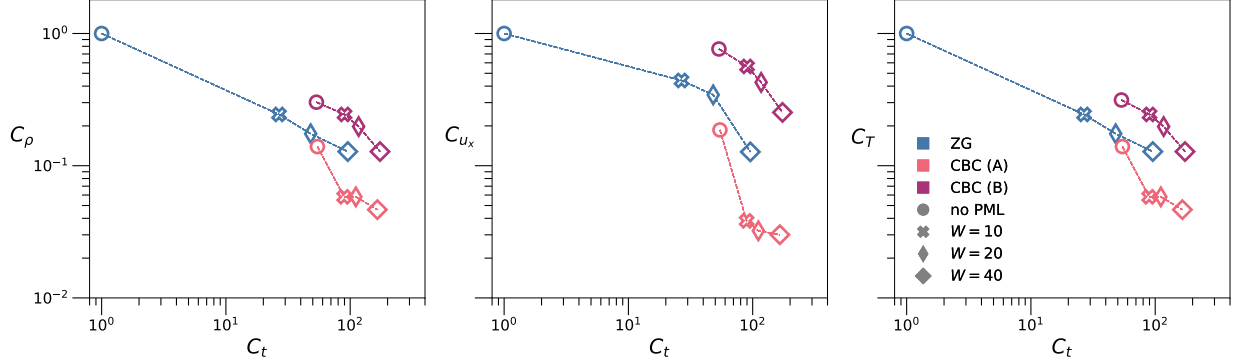


Fig. 9 Computational cost vs accuracy for the “thermal vortex” test case.

For this test-case, the computational time required for applying characteristic BCs increases the time spent in the boundary routine by a factor of about 50. This is because all boundaries are taken to be open, and the characteristic BCs must also account for the energy equation in this thermal flow configuration, which increases the method’s overhead compared to simple extrapolation.

As a result, the computational cost for evolving the fluid in the PML region is not as dominant as was in the previous benchmark. Using CBC beyond a PML with a width $W = 20$ is about as costly as using a Zero Gradient (ZG) BC with $W = 40$. While CBCs are more expensive than ZG BCs, they are still more accurate at a comparable computational cost.

However, the choice of the parameters of the CBC is critical to preserve the advantages over the ZG BC. This is shown by comparing the choice for how the incoming wave amplitudes are handled by the two different CBC schemes. The perfectly non-reflecting CBC (scheme B), where incoming wave amplitudes are set to zero, produces less accurate results and requires more runtime than the ZG BC with PML. The relaxation of incoming wave amplitudes as described in Eq. (27) (scheme A), on the other hand, allows to minimize the error for all the macroscopic fields.

In conclusion, the combination of characteristic BCs and PML can be a more efficient choice than the ZG BC with PML if a high level of accuracy is required. However, this requires careful tuning of parameters for both the PML and the characteristic BC. If the accuracy levels obtained using the ZG BC beyond the PML are sufficient, the ZG BC offers a simpler implementation and faster evaluation.

Finally, we note that the outlet boundary is usually the most critical for reducing reflections at open boundaries. Therefore, the damping zones at the remaining boundaries can be thinner, potentially reducing the computational overhead introduced by the PML.

VI. Conclusion

In this paper, we have revised the derivation of perfectly matched layers in the lattice Boltzmann method, and presented their implementation coupled with a non-reflective boundary condition, supporting both standard single-speed

as well as multi-speed velocity stencils. We have reported results of a few selected benchmarks to evaluate and compare the impact of using different BC in combination with the PML, both in terms of obtained accuracy and computational cost.

We have shown that for simple flow configurations with one-dimensional dynamics, characteristic BCs provide the best trade-off between accuracy and computational costs. Since their derivation assumes a locally one-dimensional dynamic, they allow to dampen the reflection waves introduced by the truncation of the computational domain, such that their combination with PML does not offer significant gains in terms of accuracy.

On the other hand, when considering flow with truly two-dimensional dynamics, even carefully tuning the parameters of the CBC leads unavoidably to reflection waves polluting the bulk domain, in turn making the coupling with PML more compelling. In this scenario, CBC coupled with PML still provides significant gains in accuracy, and at relatively modest computational overhead, than the coupling between a zero-gradient BC with PML, provided that the parameters of both CBC and PML are carefully tuned. In particular, the performance of the CBC critically depends on modeling choice performed for handling the inward pointing wave amplitude variations.

If the accuracy levels obtained using the ZG BC beyond the PML are sufficient, the ZG BC offers a simpler implementation, reducing complexity and computational costs even when using higher order LBM models based on multi-speed stencils.

Finally, the choice of the dampening coefficient σ plays a crucial role in the overall accuracy of the PML approach, however it is in general not known how this parameter should be chosen in simulations. Alongside σ , also the choice of f^{eq} might be non trivial, specially in the presence of turbulent flows. This, combined with the extra parameters that can be tweaked in the CBC formulation, makes up for a vast search space which can be explored in attempt to further improve the performances of this class of NRBC. In a future work we plan to employ a data driven approach [39, 40] for the optimization of the free parameters of the BC, and evaluate its effect in the stability of simulations of flows at increasingly large Mach numbers.

Acknowledgments

A.G. gratefully acknowledge the support of the U.S. Department of Energy through the LANL/LDRD Program under project number 20240740PRD1 and the Center for Non-Linear Studies for this work.

Appendix

A. Characteristic analysis with the Perfectly Matched Layer

In this Appendix section, we describe the possibility of defining a characteristic BC consistent with the modified governing equations that arise in the PML approach.

As discussed in the main text, the PML approach for the Lattice Boltzmann Method consists in a modified collision operator

$$\Omega_i = \Omega_i^{BGK} + \Omega_i^{\text{PML}}, \quad (\text{A.1})$$

where Ω_i^{BGK} is the BGK-collision operator and the additional term is given by

$$\Omega_i^{\text{PML}} = -\sigma \left(\mathbf{c}_i \cdot \nabla Q_i + 2\hat{f}_i^{\text{eq}} + \sigma Q_i \right). \quad (\text{A.2})$$

In the above, the quantity $\hat{f}_i^{\text{eq}} = f_i^{\text{eq}} - \bar{f}_i^{\text{eq}}$ denotes the deviation from a mean equilibrium state $\bar{f}_i^{\text{eq}} = \bar{f}_i^{\text{eq}}(\bar{\rho}, \bar{\mathbf{u}}, \bar{T})$ and the term Q_i is calculated from the relation

$$\frac{\partial Q_i}{\partial t} = \hat{f}_i^{\text{eq}}. \quad (\text{A.3})$$

Thus, usage of PML alters the macroscopic limit of the Lattice Boltzmann Equation by adding velocity moments of Eq. (A.2) to the continuity, momentum and energy equations. This effect can be expressed in terms of the conserved macroscopic quantities $\mathbf{U} = (\rho, \rho\mathbf{u}, \rho e)^\top$ and the auxiliary variables $\tilde{\mathbf{Q}}, \tilde{\mathbf{Q}}_\alpha$, which are given by [14]

$$\frac{\partial \tilde{\mathbf{Q}}}{\partial t} = \mathbf{U} - \bar{\mathbf{U}}, \quad \frac{\partial \tilde{\mathbf{Q}}_\alpha}{\partial t} = \int c_\alpha \begin{bmatrix} 1 \\ c_\beta \\ c_\beta c_\beta \end{bmatrix} [f^{\text{eq}} - \bar{f}^{\text{eq}}] dc,$$

where $\bar{\mathbf{U}} = (\bar{\rho}, \bar{\rho}\bar{\mathbf{u}}, \bar{\rho}\bar{e})^\top$ labels the conserved quantities corresponding to the mean equilibrium \bar{f}^{eq} .

In conclusion, instead of using Eq. (18) as starting point for the definition of the characteristic analysis we can use instead

$$\frac{\partial \mathbf{U}}{\partial t} = -A \frac{\partial \mathbf{U}}{\partial x} + \mathbb{T} + \mathbb{V} + \mathbb{S} \left(\underbrace{\sigma \left(\frac{\partial \tilde{\mathbf{Q}}_x}{\partial x} + \frac{\partial \tilde{\mathbf{Q}}_y}{\partial y} \right)}_I + \underbrace{2\sigma (\mathbf{U} - \bar{\mathbf{U}})}_{II} + \underbrace{\sigma^2 \tilde{\mathbf{Q}}}_{III} \right), \quad (\text{A.4})$$

where $\mathbb{S} = \frac{1}{\rho} \left(\rho, 1, \frac{d}{2} \right)^\top$ is a scaling vector used to relate primitive to conserved variables.

The characteristic analysis now follows the same steps as described in Sec. IV, the only difference is the presence of the additional source terms.

We consider once again the one-dimensional density step case described in the main text (cf. Sec. V.A). In Fig. A.1, we compare the time evolution of the global error for this new combined LODI-PML, evaluating the effect of including different combinations of the extra terms present in Eq.A.4. All cases make use of a PML of width $W = 10$ and $\sigma_{\text{max}} = 0.001$.

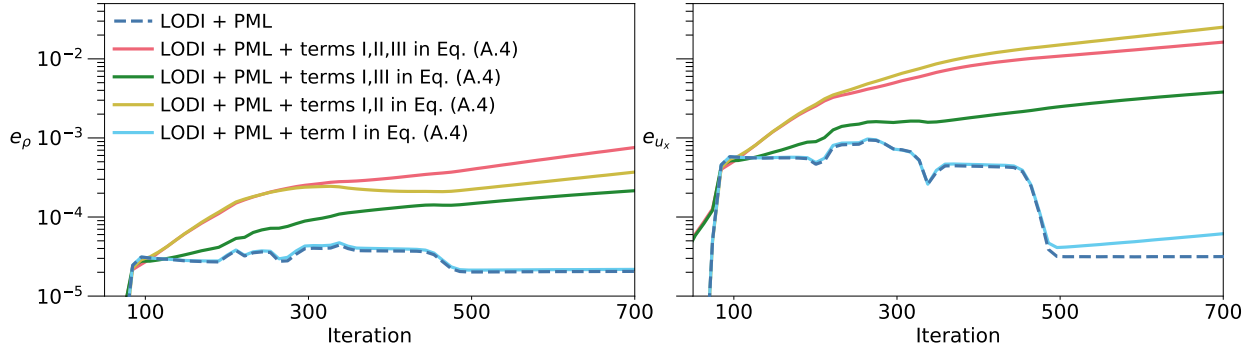


Fig. A.1 Evolution of global errors in the isothermal step benchmark on incorporation of the moments of the modified collision operator (A.4) in the LODI BC (22).

We observe that this new approach gives comparable accuracy to the combined LODI-PML approach previously presented in the main text only when discarding the second and third additional terms in Eq.A.4. Other combinations yields a significant decrease in the obtained accuracy. We speculate that the reason for this comes from the choice of the mean equilibrium state \bar{f}_i^{eq} , which is here non time/space dependent, and we leave as a open problem the definition of an optimal choice for \bar{f}_i^{eq} .

References

- [1] Berenger, J.-P., “A perfectly matched layer for the absorption of electromagnetic waves,” *Journal of Computational Physics*, Vol. 114, No. 2, 1994, pp. 185–200. <https://doi.org/10.1006/jcph.1994.1159>.
- [2] Collino, F., and Tsogka, C., “Application of the perfectly matched absorbing layer model to the linear elastodynamic problem in anisotropic heterogeneous media,” *GEOPHYSICS*, Vol. 66, No. 1, 2001, pp. 294–307. <https://doi.org/10.1190/1.1444908>.
- [3] Antoine, X., Arnold, A., Besse, C., Ehrhardt, M., and Schädle, A., “A Review of Transparent and Artificial Boundary Conditions Techniques for Linear and Nonlinear Schrödinger Equations,” *Communications in Computational Physics*, Vol. 4, 2008, pp. 729–796. URL http://global-sci.org/intro/article_detail/cicp/7814.html.
- [4] Singer, I., and Turkel, E., “A perfectly matched layer for the Helmholtz equation in a semi-infinite strip,” *Journal of Computational Physics*, Vol. 201, No. 2, 2004, pp. 439–465. <https://doi.org/10.1016/j.jcp.2004.06.010>.
- [5] Hu, F. Q., “On Absorbing Boundary Conditions for Linearized Euler Equations by a Perfectly Matched Layer,” *Journal of Computational Physics*, Vol. 129, No. 1, 1996, pp. 201–219. <https://doi.org/10.1006/jcph.1996.0244>.
- [6] Hu, F., “On perfectly matched layer as an absorbing boundary condition,” *Aeroacoustics Conference*, 1996, p. 1664. <https://doi.org/10.2514/6.1996-1664>.
- [7] Hu, F. Q., “A Stable, Perfectly Matched Layer for Linearized Euler Equations in Unsplit Physical Variables,” *Journal of Computational Physics*, Vol. 173, No. 2, 2001, pp. 455–480. <https://doi.org/10.1006/jcph.2001.6887>.

- [8] Hagstrom, T., Goodrich, J., Nazarov, I., and Dodson, C., “High-order methods and boundary conditions for simulating subsonic flows,” *11th AIAA/CEAS Aeroacoustics Conference*, 2005, p. 2869. <https://doi.org/10.2514/6.2005-2869>.
- [9] Hagstrom, T., and Appelo, D., “Experiments with Hermite methods for simulating compressible flows: Runge-Kutta time-stepping and absorbing layers,” *13th AIAA/CEAS Aeroacoustics Conference (28th AIAA Aeroacoustics Conference)*, 2007, p. 3505. <https://doi.org/10.2514/6.2007-3505>.
- [10] Hu, F. Q., Li, X., and Lin, D., “Absorbing boundary conditions for nonlinear Euler and Navier–Stokes equations based on the perfectly matched layer technique,” *Journal of Computational Physics*, Vol. 227, No. 9, 2008, pp. 4398–4424. <https://doi.org/10.1016/j.jcp.2008.01.010>.
- [11] Hu, F. Q., and Craig, E., “On the Perfectly Matched Layer for the Boltzmann-BGK Equation and its Application to Computational Aeroacoustics,” *16th AIAA/CEAS Aeroacoustics Conference*, American Institute of Aeronautics and Astronautics, 2010. <https://doi.org/10.2514/6.2010-3935>.
- [12] Sutti, M., and Hesthaven, J. S., “Perfectly matched layers for the Boltzmann equation: Stability and sensitivity analysis,” *Journal of Computational Physics*, Vol. 509, 2024, p. 113047. <https://doi.org/10.1016/j.jcp.2024.113047>.
- [13] Tekitek, M., Bouzidi, M., Dubois, F., and Lallemand, P., “Towards perfectly matching layers for lattice Boltzmann equation,” *Computers & Mathematics with Applications*, Vol. 58, No. 5, 2009, pp. 903–913. <https://doi.org/10.1016/j.camwa.2009.02.013>.
- [14] Najafi-Yazdi, A., and Mongeau, L., “An absorbing boundary condition for the lattice Boltzmann method based on the perfectly matched layer,” *Computers & Fluids*, Vol. 68, 2012, pp. 203–218. <https://doi.org/10.1016/j.compfluid.2012.07.017>.
- [15] Shao, W., and Li, J., “An Absorbing Boundary Condition Based on Perfectly Matched Layer Technique Combined with Discontinuous Galerkin Boltzmann Method for Low Mach Number Flow Noise,” *Journal of Theoretical and Computational Acoustics*, Vol. 26, No. 04, 2018, p. 1850011. <https://doi.org/10.1142/s2591728518500111>.
- [16] Poinso, T., and Lele, S., “Boundary conditions for direct simulations of compressible viscous flows,” *Journal of Computational Physics*, Vol. 101, No. 1, 1992, pp. 104–129. [https://doi.org/10.1016/0021-9991\(92\)90046-2](https://doi.org/10.1016/0021-9991(92)90046-2).
- [17] Colonius, T., Lele, S. K., and Moin, P., “Boundary conditions for direct computation of aerodynamic sound generation,” *AIAA Journal*, Vol. 31, No. 9, 1993, pp. 1574–1582. <https://doi.org/10.2514/3.11817>.
- [18] Freund, J. B., “Proposed Inflow/Outflow Boundary Condition for Direct Computation of Aerodynamic Sound,” *AIAA Journal*, Vol. 35, No. 4, 1997, pp. 740–742. <https://doi.org/10.2514/2.167>.
- [19] Chen, Y., and Xuan, Y., “Lattice Boltzmann approach for near-field thermal radiation,” *Physical Review E*, Vol. 102, No. 4, 2020. <https://doi.org/10.1103/physreve.102.043308>.
- [20] Rajamuni, M. M., Liu, Z., Wang, L., Ravi, S., Young, J., Lai, J. C. S., and Tian, F.-B., “An Immersed Boundary-Regularised Lattice Boltzmann Method for Modelling Fluid-Structure-Acoustics Interactions Involving Large Deformation,” 2023. <https://doi.org/10.2139/ssrn.4624793>.

- [21] Chen, X., Yang, K., and Shan, X., “Characteristic boundary condition for multispeed lattice Boltzmann model in acoustic problems,” *Journal of Computational Physics*, 2023, p. 112302. <https://doi.org/10.1016/j.jcp.2023.112302>.
- [22] Shan, X., Yuan, X.-F., and Chen, H., “Kinetic theory representation of hydrodynamics: a way beyond the Navier-Stokes equation,” *Journal of Fluid Mechanics*, Vol. 550, 2006, pp. 413–441. <https://doi.org/10.1017/S0022112005008153>.
- [23] Shan, X., “General solution of lattices for Cartesian lattice Bhatnagar-Gross-Krook models,” *Physical Review E*, Vol. 81, 2010, p. 036702. <https://doi.org/10.1103/PhysRevE.81.036702>.
- [24] Krüger, T., Kusumaatmaja, H., Kuzmin, A., Shardt, O., Silva, G., and Viggen, E. M., *The Lattice Boltzmann Method*, Springer International Publishing, 2017. <https://doi.org/10.1007/978-3-319-44649-3>.
- [25] Succi, S., *The Lattice Boltzmann Equation: For Complex States of Flowing Matter*, OUP Oxford, 2018. <https://doi.org/10.1093/oso/9780199592357.001.0001>.
- [26] Bhatnagar, P. L., Gross, E. P., and Krook, M., “A Model for Collision Processes in Gases. Amplitude Processes in Charged and Neutral One-Component Systems,” *Physical review*, Vol. 94, No. 3, 1954, pp. 511–525. <https://doi.org/10.1103/PhysRev.94.511>.
- [27] Chapman, S., and Cowling, T. G., *The Mathematical Theory of Non-Uniform Gases*, 3rd ed, 3rd ed., Cambridge Mathematical Library, Cambridge University Press, 1990. URL <https://books.google.de/books?id=y2Yyy798WzIC>.
- [28] Shan, X., “The mathematical structure of the lattices of the lattice Boltzmann method,” *Journal of Computational Science*, Vol. 17, 2016, pp. 475–481. <https://doi.org/10.1016/j.jocs.2016.03.002>.
- [29] Philippi, P. C., Hegele, L. A., dos Santos, L. O. E., and Surmas, R., “From the continuous to the lattice Boltzmann equation: The discretization problem and thermal models,” *Physical Review E*, Vol. 73, No. 5, 2006. <https://doi.org/10.1103/physreve.73.056702>.
- [30] Modave, A., Delhez, E., and Geuzaine, C., “Optimizing perfectly matched layers in discrete contexts,” *International Journal for Numerical Methods in Engineering*, Vol. 99, No. 6, 2014, pp. 410–437. <https://doi.org/10.1002/nme.4690>.
- [31] Klass, F., Gabbana, A., and Bartel, A., “A Characteristic Boundary Condition for Multispeed Lattice Boltzmann Methods,” *Communications in Computational Physics*, Vol. 33, No. 1, 2023, pp. 101–117. <https://doi.org/10.4208/cicp.oa-2022-0052>.
- [32] Klass, F., Gabbana, A., and Bartel, A., “Characteristic boundary condition for thermal lattice Boltzmann methods,” *Computers & Mathematics with Applications*, Vol. 157, 2024, pp. 195–208. <https://doi.org/10.1016/j.camwa.2023.12.033>.
- [33] Thompson, K. W., “Time dependent boundary conditions for hyperbolic systems,” *Journal of Computational Physics*, Vol. 68, No. 1, 1987, pp. 1–24. [https://doi.org/10.1016/0021-9991\(87\)90041-6](https://doi.org/10.1016/0021-9991(87)90041-6).
- [34] Yoo, C. S., Wang, Y., Trouvé, A., and Im, H. G., “Characteristic boundary conditions for direct simulations of turbulent counterflow flames,” *Combustion Theory and Modelling*, Vol. 9, No. 4, 2005, pp. 617–646. <https://doi.org/10.1080/13647830500307378>.

- [35] Jung, N., Seo, H. W., and Yoo, C. S., “Two-dimensional characteristic boundary conditions for open boundaries in the lattice Boltzmann methods,” *Journal of Computational Physics*, Vol. 302, 2015, pp. 191–199. <https://doi.org/10.1016/j.jcp.2015.08.044>.
- [36] Heubes, D., Bartel, A., and Ehrhardt, M., “Characteristic boundary conditions in the lattice Boltzmann method for fluid and gas dynamics,” *Journal of Computational and Applied Mathematics*, Vol. 262, 2014, pp. 51–61. <https://doi.org/10.1016/j.cam.2013.09.019>.
- [37] Klass, F., Gabbana, A., and Bartel, A., “A non-equilibrium bounce-back boundary condition for thermal multispeed LBM,” *Journal of Computational Science*, Vol. 53, 2021, p. 101364. <https://doi.org/10.1016/j.jocs.2021.101364>.
- [38] Yoo, C. S., and Im, H. G., “Characteristic boundary conditions for simulations of compressible reacting flows with multi-dimensional, viscous and reaction effects,” *Combustion Theory and Modelling*, Vol. 11, No. 2, 2007, pp. 259–286. <https://doi.org/10.1080/13647830600898995>.
- [39] Bedrunka, M. C., Wilde, D., Kliemank, M., Reith, D., Foysi, H., and Krämer, A., “Lettuce: PyTorch-Based Lattice Boltzmann Framework,” Springer International Publishing, Cham, 2021, pp. 40–55. https://doi.org/10.1007/978-3-030-90539-2_3.
- [40] Corbetta, A., Gabbana, A., Gyrya, V., Livescu, D., Prins, J., and Toschi, F., “Toward learning Lattice Boltzmann collision operators,” *The European Physical Journal E*, Vol. 46, No. 3, 2023, p. 10. <https://doi.org/10.1140/epje/s10189-023-00267-w>.